

# Validation and Verification of Aerospike Designs in Supersonic Flow

Ishar Singh Saini<sup>1</sup>

<sup>1</sup>Department of Aerospace Engineering, Amity University Mumbai, Panvel, Maharashtra

Mentor: Dr. Tushar Chourushi<sup>2</sup>

<sup>2</sup>Assistant Professor in Aerospace Engineering, Amity University Mumbai, Panvel, Maharashtra

## ABSTRACT

This project aims to simulate the supersonic/hypersonic flow over an aerospike blunt body using the SonicFoam solver which is part of the open-source software OpenFOAM and verify the obtained aerodynamic forces with the available results. The use of a blunt shape considerably reduces aero heating over the missiles and blunt shaped bodies but leads to increased drag. To avoid this, an aerospike becomes very useful to create a detached shock ahead of the body, reducing the aerodynamic drag of blunt bodies at supersonic or hypersonic speeds. Thus, modifying high-speed flight vehicles by adding a spike attached to the stagnation point drastically increases efficiency. The length of the aerospike is set equivalent to the base diameter of the cylinder (body). Numerical simulations are performed by keeping a constant Reynolds Number at  $0.23 \times 10^6$  and varying the Mach numbers.

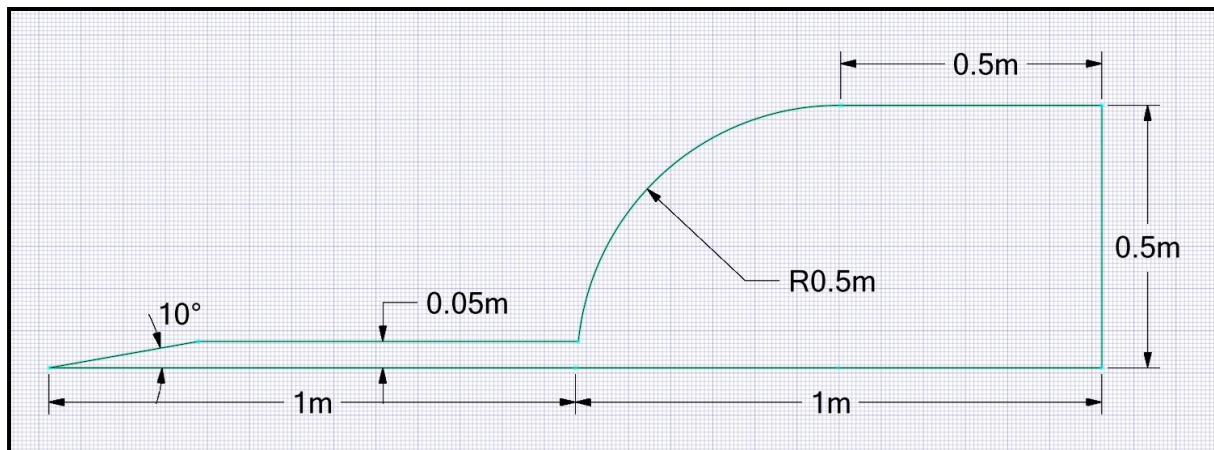


**Figure 1. Details of Blunt Body with Aerospike Geometry**

### Reference Paper:

David H. Crawford's research paper – 'Investigation of the flow over a spiked-nose hemispherical cylinder', 1959.

# Contents

1. Introduction	(1)
2. Aerodynamic Effects at Supersonic Speeds – An overview	(2)
2.1 Introduction	(2)
2.2 Drag Effects	(3)
2.3 Shock Waves	(3)
2.3.1 Bow Shock	(3)
2.3.2 Conical Shock	(3)
2.4 Aerodynamic Heating	(4)
3. Theory	(5)
3.1 Solver and Governing Equations	(5)
3.2 Turbulence Modelling	(5)
3.3 Previous Work and Data	(6)
3.4 Geometry	(7)
3.5 Solver Setup and Boundary Conditions	(8)
3.6 Meshing	(10)
3.6.1 Blunt Body	(10)
3.6.2 Blunt Body with Aerospike	(11)
3.6.3 Mesh Quality	(12)
3.7 Grid Independence Study	(12)
4. Results	(14)
4.1 Comparison between Compressible solvers	(14)
4.2 Validation and Verification	(15)
4.3 Shock/Density Contours	(15)
4.4 Velocity over the body	(17)
4.5 Temperature	(18)
4.6 Pressure Distribution	(19)
4.7 Drag Forces	(21)
5. Conclusion	(23)
5.1 Conclusion	(23)
5.2 Note on OpenFoam's Compressible Solvers	(23)
5.2 Future Scope	(23)

## List of Figures

1. Details of Blunt Body with Aerospike Geometry	
1.1 Shock Wave formations over Blunt and Spiked Blunt Body	(1)
3.1 Crawford's experimental apparatus geometry	(6)
3.2 David Crawford's $C_D$ vs $L/D$ plot	(7)
3.3 Blunt Body Geometry	(7)
3.4 Blunt Body with Spike Geometry	(8)
3.5 Boundary Conditions Schematic	(9)
3.6 Mesh for Blunt Body	(10)
3.7 Close-up view for Blunt Body with different coloured blocking	(10)
3.8 Mesh for Blunt Body with Aerospike	(11)
3.9 Close-up view for Blunt Body with spike with different coloured blocking	(11)
3.10 Close-up view on the pointed spike	(11)
4.1 rhoPimpleFoam (A) and sonicFoam's (B) Residual Plots	(14)
4.2 Side by side comparison of shock waves for Crawford's experiment and sonicFoam	
4.3 Density Contours for Blunt and Spiked Blunt Bodies at different Mach numbers.	(16)
4.4 Velocity Contours for Blunt and Spiked Blunt Bodies at different Mach numbers.	(17)
4.5 Temperature Contours for Blunt and Spiked Blunt Bodies at different Mach numbers.	
4.6 Pressure Contours for Blunt and Spiked Blunt Bodies at different Mach numbers.	
4.7 $P/P_\infty$ vs X co-ordinates Plot for different velocities	(20)
4.8 $C_D$ vs $L/D$ Plot	(21)
4.9 Drag Force vs $L/D$ Plot	(22)

## List of Tables

1. Constant Parameters	(8)
2. Varied Parameters	(8)
3. Boundary Conditions	(9)
4. Drag Force Variation in Grid Independence	(13)
5. Comparison in Drag Coefficient Results	(14)

# Chapter 1

## Introduction

Many re-entry vehicles and hypersonic/supersonic aircrafts always encounter the problem of aerodynamic heating and drag at such high-speeds. Engineers and scientists aim to encounter these problems by various methods. Generally, a blunt body is used for dissipating heat and is considered a great shape for overcoming heat transfer issues. There are various types of drag reduction approaches that are used nowadays, including aerospike, counterflow, and energy deposition [11]. We are going to consider the aerospike approach for our current work.

An aerospike attached to the front of the body detaches the shock wave prior to reaching the main body thereby reducing drag by this detached conical shock. This reduces fuel consumption and also increases the aerodynamic performance of the flight [9]. As we can see from Figure 1.1, we can get a clear visualization of how this drag-reduction phenomena works.

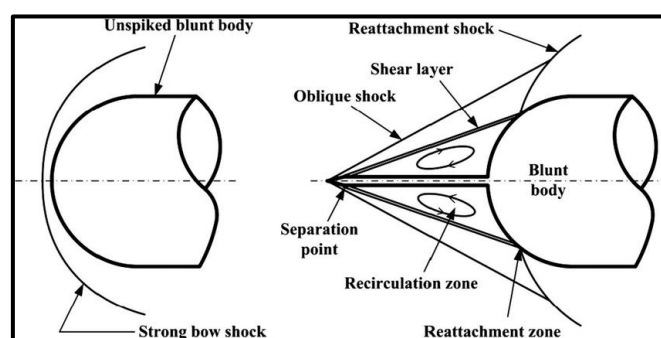


Figure 1.1 Shock Wave formations over Blunt and Spiked Blunt Body

The figure 1.1 shows a bow shock formation away from the blunt body. But when the spike is attached at the front, it creates a conical shock instead of the bow shock, thereby reducing drag. [15][12]

D. Crawford's [1] experimental data and studies measures the drag and heat transfer around a hemispheric cylindrical blunt body with pointed aerospike at the speed of Mach 6.8 at various Reynold's numbers. and found that varying the length has a significant effect on heat flux but it doesn't have any influence on drag reduction when the length exceeds by roughly four times of the blunt body diameter. First, we try to validate the experimental data using CFD.

## Chapter 2

# Aerodynamic Effects at Supersonic Speeds – An overview

### 2.1 Introduction

The aerodynamic behaviour undergoes a significant transformation when objects move at supersonic speeds, which exceed the speed of sound in air. Supersonic flight introduces a multitude of complex aerodynamic effects that challenges the industry of aerospace. Supersonic flight, typically defined as Mach numbers (the ratio of an object's speed to the speed of sound) greater than 1, is quite different from normal subsonic flows. As an object accelerates beyond the speed of sound (Mach 1), it enters a new domain where shock waves, compressibility effects are significant. These effects profoundly impact the performance, stability, and controllability of aircraft and spacecraft operating in the supersonic regime. Whereas in hypersonic flows ( $Ma > 5$ ) heating affects becomes an additional challenge.

One of the most striking features of supersonic aerodynamics is the presence of shock waves. Shock waves are intense, localized pressure and density changes that form as a consequence of the abrupt compression of air when it encounters an object traveling faster than sound. These shock waves produce a series of remarkable phenomena, including the formation of a bow shock in front of the supersonic object and a conical shock wave pattern trailing behind it. Understanding and managing these shock waves is crucial for designing efficient and safe supersonic vehicles.

### 2.2 Drag Effects

Understanding and managing drag is a fundamental challenge in the design and operation of high-speed aircrafts, particularly at high Mach numbers. Drag is the aerodynamic force that opposes the motion of an object through a fluid, such as air, and it plays a crucial role in determining an object's speed, efficiency, and fuel consumption. At supersonic and hypersonic speeds, drag behaves differently compared to subsonic flight.

At high Mach numbers the inertial forces are much dominant than the viscous forces so many times CFD researchers and engineers consider flows to be inviscid due to this dominance. But in our case, we aim to maintain the  $Re$  at  $0.23 \times 10^6$ . Thus, we do not consider the flow to be inviscid.

Here, the we compare our aerodynamic drag results in terms of **drag coefficient**.

$$C_D = \frac{2D}{\rho_{\infty} V_{\infty}^2 A}$$

where  $C_D$  = Drag Coefficient

$D$  = Drag Force

$\rho_{\infty}$  = Free-stream Density

$V_{\infty}$  = Free-stream Velocity

$A$  = Reference Area

(Note: In our 3D case the reference area is the frontal projected area which is the circle.)

## 2.3 Shock Waves

Shock is a compression front across which the flow properties jump. Shock may also be described as a front in a supersonic flow field, and the flow processing across the front results in an abrupt change in fluid properties. In other words, shock is a thin region where large gradients in temperature, pressure, and velocity occur and where the transport phenomena of momentum and energy are important. The thickness of the shocks is comparable to the mean free path of the gas molecules in the flow field.

### 2.3.1 Bow Shock/Normal Shock

A bow shock forms when an object moves through a fluid at a speed greater than the speed of sound in that fluid ( $Ma > 1$ ). As the object travels through the fluid, it displaces air molecules in front of it. The air molecules cannot react instantaneously to this displacement due to their finite speed of propagation. Consequently, a high-pressure region builds up in front of the object, leading to the formation of a curved shock wave known as a bow shock. The bow shock creates a boundary between the supersonic flow around the object and the undisturbed fluid ahead of it. This type of shock is observed on the blunt body.

### 2.3.2 Conical Shock

These are also a normal shock but are a specific type of shock wave that precedes the body as it moves through a fluid at velocities exceeding the local speed of sound. They are a result of the abrupt compression of air molecules in front of an object moving faster than the speed of sound. As the object advances through the fluid, it generates a high-pressure region in front of it. This high-pressure region cannot "communicate" the object's presence to adjacent air molecules instantaneously because information in the fluid travels at the speed of sound. Therefore, a shock wave begins to develop ahead of the object. The cone angle of the shock depends on the speed of free-stream. If the free-stream at the speed of sound, the angle will be  $90^\circ$ . We observe this type of shock at the front of the spike and usually behind the body.

The main difference in these two formations is due to the stagnation pressure at the front.

## 2.4 Aerodynamic Heating

Aerodynamic heating is a critical consideration for objects traveling at high Mach numbers. When an object moves at such velocities, it encounters significant aerodynamic heating due to the interaction between the object and the surrounding air. This phenomenon is especially pronounced at hypersonic Mach numbers ( $Ma > 5$ ) and has significant implications for the body design.

At such high Mach numbers, the behaviour of air changes significantly. Air can no longer be considered incompressible, as it is at subsonic speeds. Instead, the air molecules experience substantial compression and heating as they are forced to move at high speeds. These compressibility effects lead to a rise in air temperature and pressure around the object and thus formation of shocks as discussed earlier. When the high-pressure air is forced to slow down and come to a stop, it undergoes adiabatic compression, causing a significant increase in its temperature. This process is known as compression heating.

There are also frictional forces due to the collision of air molecules with the object's surface. The kinetic energy of the high-speed air molecules is transferred to the object's surface as heat. The intense heating generated by frictional forces can lead to very high temperatures on the object's surface. The heating part is the major problem re-entry space vehicles and hypersonic aircrafts face during their operations.



## Chapter 3

### Theory

#### 3.1 Solver and Governing Equations

SonicFoam is a Transient solver for trans-sonic/supersonic, turbulent flow of a compressible gas that uses PIMPLE algorithm in this case to solve the equations. The PIMPLE Algorithm is a combination of PISO (Pressure Implicit with Splitting of Operator) and SIMPLE (Semi-Implicit Method for Pressure-Linked Equations). The flow regime in this case is mainly governed by equations;

- Mass Continuity

$$\frac{\partial \rho}{\partial t} + \nabla \cdot (\rho \mathbf{U}) = 0 \quad (3.1)$$

- Momentum Continuity for Newtonian Fluid

$$\frac{\partial \rho \mathbf{U}}{\partial t} + \nabla \cdot (\rho \mathbf{U} \mathbf{U}) - \nabla \cdot (\mu \nabla \mathbf{U}) = -\nabla p \quad (3.2)$$

- Energy Equation for fluids,  $e = C_v T$ , with Fourier's Law  $q = -k \nabla T$

$$\frac{\partial \rho e}{\partial t} + \nabla \cdot (\rho \mathbf{U} e) - \nabla \cdot \left( \frac{k}{C_v} \nabla e \right) = p \nabla \cdot \mathbf{U} \quad (3.3)$$

- Ideal Gas Law

$$p = \rho R T \quad (3.4)$$

SonicFoam solver is typically used to solve high Mach number cases which involves analysis of shock wave formations and aerodynamic drag on bodies.

#### 3.2 Turbulence Modeling

Standard K-epsilon turbulence model was used in this case. It is a Two transport equation linear-eddy-viscosity turbulence closure model where the two transport variables are turbulent kinetic energy,  $k$  and turbulent kinetic energy dissipation rate,  $\epsilon$ . The **turbulent kinetic energy** equation,  $k$ :

$$\frac{D}{Dt}(\rho k) = \nabla \cdot (\rho D_k \nabla k) + P - \rho \epsilon$$

The **turbulent kinetic energy dissipation** rate equation,  $\epsilon$ :

$$\frac{D}{Dt}(\rho \epsilon) = \nabla \cdot (\rho D_\epsilon \nabla \epsilon) + \frac{C_1 \epsilon}{k} (P + C_3 \frac{2}{3} k \nabla \cdot \mathbf{u}) - C_2 \rho \frac{\epsilon^2}{k}$$

The **turbulent viscosity** equation,  $\nu_t$

$$\nu_t = C_\mu \frac{k^2}{\epsilon}$$

Standard K-epsilon turbulence model was used in this case. It is a Two transport equation linear-eddy-viscosity turbulence closure model where the two transport are  $k$  and  $\epsilon$ .

Further, from the work of Versteeg [17], the values for a few specific constants like  $C_\mu$ ,  $C_1$ ,  $C_2$ , have been set. For calculating turbulent intensity (I), the formula for a fully developed pipe flow is used.

$$I = 0.16 \times Re^{(-\frac{1}{8})}$$

For our case, I will be around 0.034 ~ 3%. This is used to calculate various k and  $\epsilon$  values for various velocities.

For isotropic turbulence, the turbulent kinetic energy can be estimated by:

$$k = \frac{3}{2} (I |u_{ref}|)^2$$

where,  $u_{ref}$  is reference flow speed.

For isotropic turbulence, the turbulence dissipation rate can be estimated by:

$$\epsilon = \frac{C_\mu^{0.75} k^{1.5}}{L}$$

where,  $C_\mu$  is model constant equal to 0.09 by default

$L$  is reference length (m)

### 3.3 Previous Work and Data

David Crawford's [1] experimental work on blunt bodies has been conducted at Mach 6.8 at various Reynold's numbers to study the shock waves and heat transfers among the bodies.

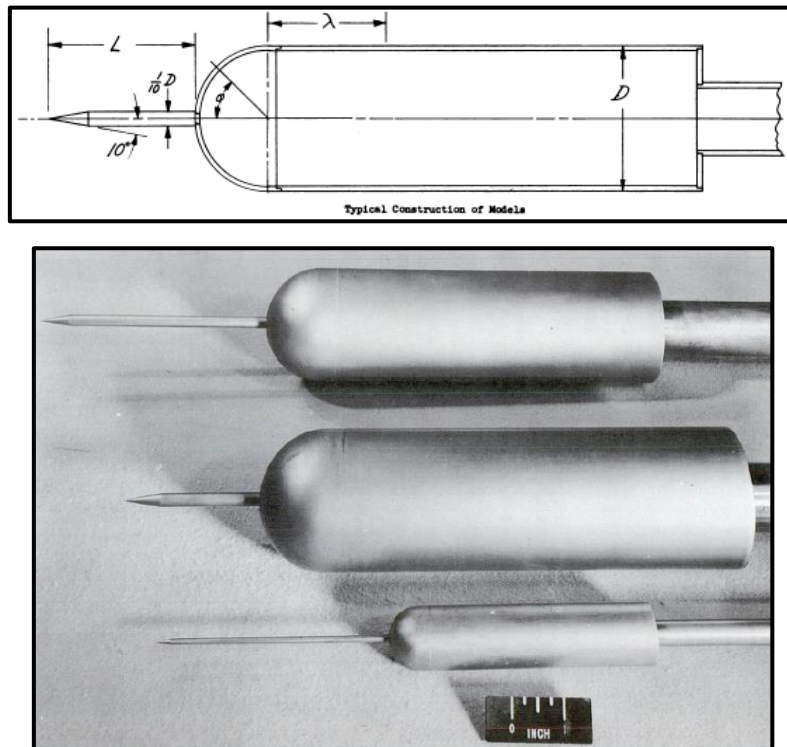


Figure 3.1: Crawford's [1] experimental apparatus geometry

We have validated their work in this paper specifically for Reynold's number  $0.23 \times 10^6$ . We refer the Figure 3.1 for the  $C_D$  values along the line for our required Re number with the diamond sign ( $\diamond$ ).

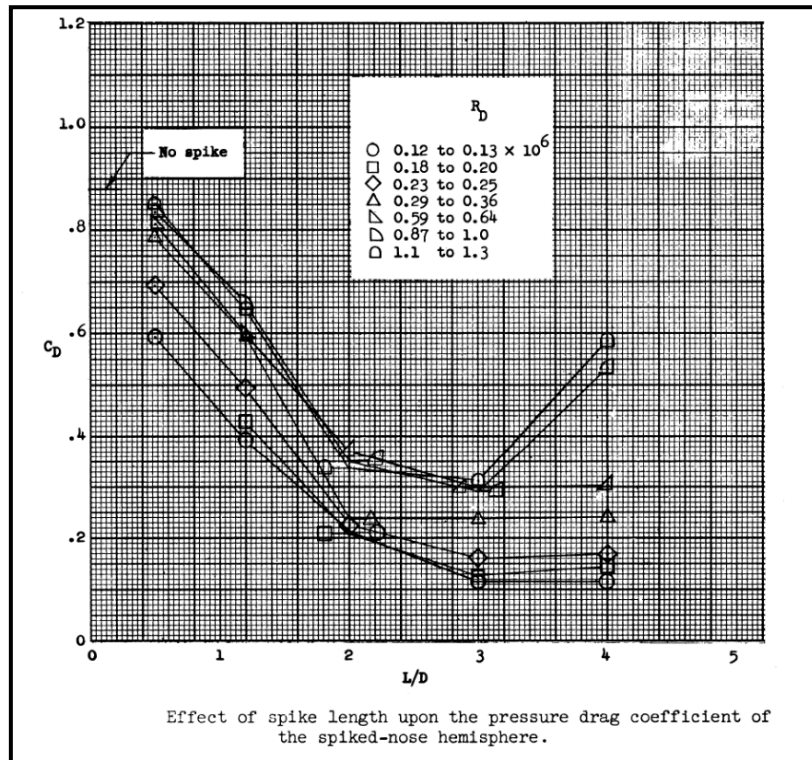


Figure 3.2 David Crawford's [1]  $C_D$  vs  $L/D$  plot

### 3.4 Geometry

There are 2 geometries mainly used in all of the simulations, namely the blunt body and the blunt body with spike. Various domain types are used for different studies. Here, we have went for C-type domain for both the geometries. Both of these 3D geometries were made in Ansys Design Modeller. (Note: Only half the geometry is represented to show the domain as the body is symmetric.)

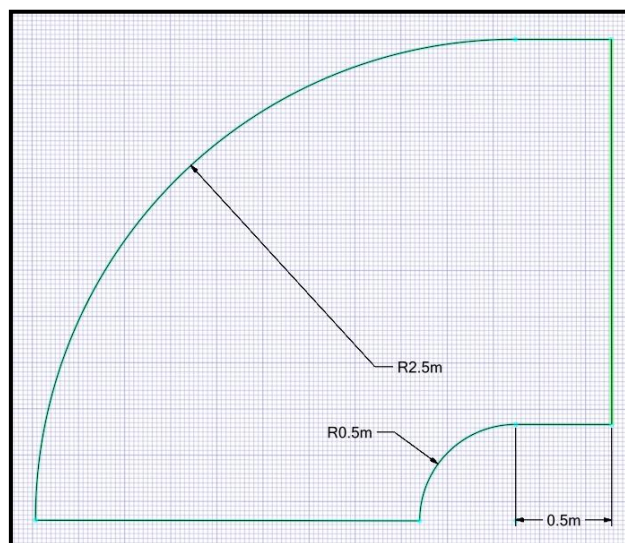


Figure 3.3 Blunt Body Geometry

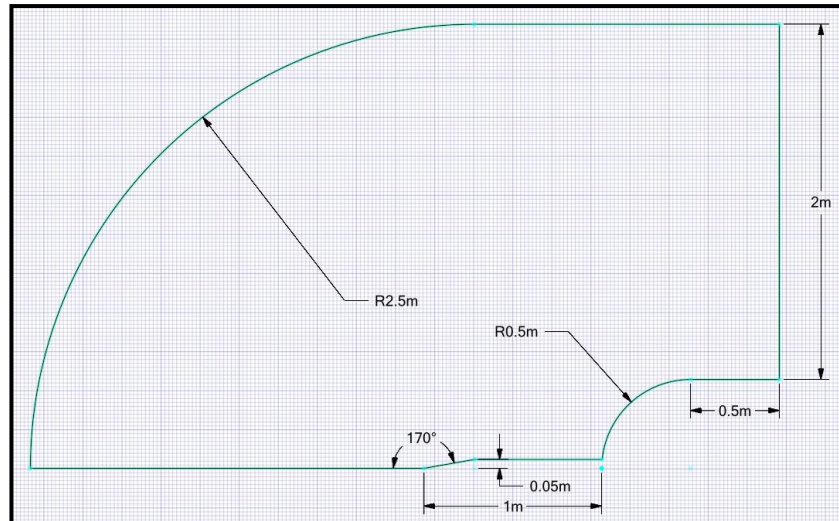


Figure 3.4 Blunt Body with Spike Geometry

### 3.5 Solver Setup and Boundary Conditions

There are three different velocity cases namely for the validation case Mach 6.82, then Mach 5, and Mach 3 were run for the blunt body as well as for the spiked body. The parameters that were **constant** for all the cases are:

Parameters	Values
Reynold's number	$0.23 \times 10^6$
Density	$1.176407 \text{ kg/m}^3$
Pressure	$101325 \text{ Pa}$
Temperature	$300 \text{ K}$

Table 1: Constant Parameters

(Note: For calculating  $Re$ , the reference length  $L$ , has been taken 1 m for both the geometries.) The pressure and temperature values are assumed to be standard atmospheric conditions as it has not been mentioned clearly in Crawford's paper [1].

For the different velocities, the dynamic viscosity  $\mu$  has been **varied** to keep our Reynold's number. constant.

Velocity	Dynamic viscosity $\mu$
Ma 6.82 / 2339.26 m/s	$0.011965 \text{ N.s/m}^2$
Ma 5 / 1715 m/s	$0.008772 \text{ N.s/m}^2$
Ma 3 / 1029 m/s	$0.005263 \text{ N.s/m}^2$

Table 2: Varied Parameters

The following table shows the different patch types used for various parameters for the initial conditions.



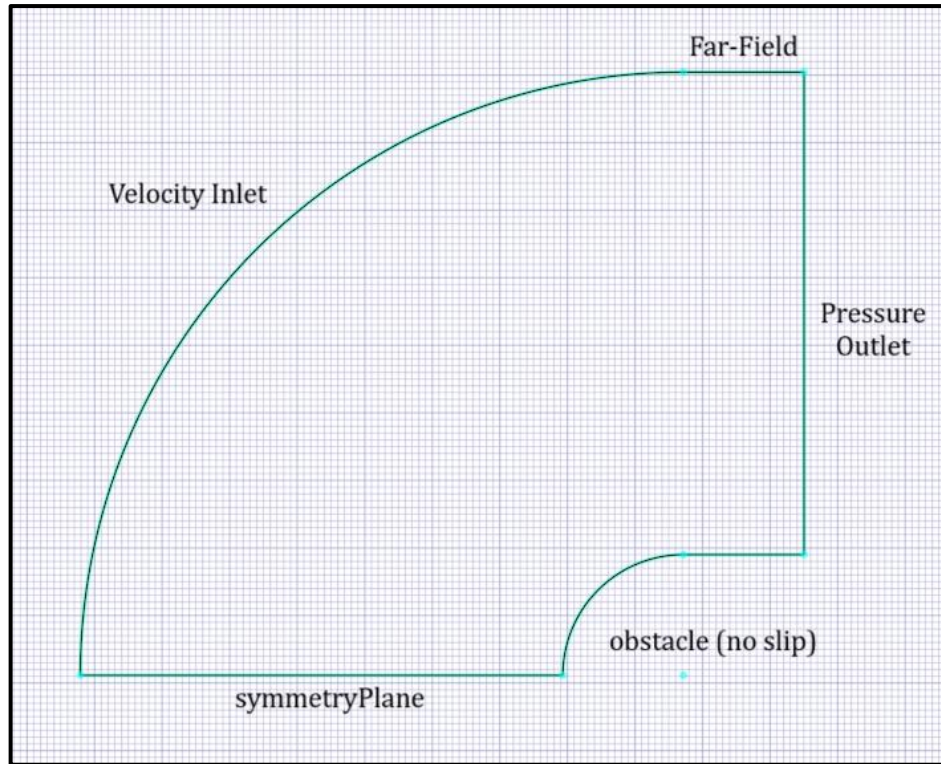


Figure 3.5: Boundary Conditions Schematic

Variable	Inlet	Outlet	FarField	Obstacle	SymmetryPlane
<b>Pressure</b>	fixedValue	waveTransmissive (non-reflective)	zeroGradient	zeroGradient	symmetryPlane
<b>Velocity</b>	fixedValue	inletOutlet	supersonicFreestream	noSlip	symmetryPlane
<b>Temp</b>	fixedValue	inletOutlet	inletOutlet	zeroGradient	symmetryPlane
$\alpha_T$	calculated	calculated	calculated	alphiatWallFunction	symmetryPlane
$\epsilon$	fixedValue	inletOutlet	inletOutlet	epsilonWallFunction	symmetryPlane
<b>K</b>	fixedValue	inletOutlet	inletOutlet	kqRWallFunction	symmetryPlane
<b>v</b>	calculated	calculated	calculated	nutkWallFunction	symmetryPlane

Table 3: Boundary Conditions

Where, for all the turbulence related terms, their respective wall functions are used at the obstacle. Figure 3. shows the boundary conditions in the schematic.

## 3.6 Meshing

Structured meshes were produced in Ansys Mesh Modeler for both the geometries.

### 3.6.1 Blunt Body

The 3D grid for the blunt body has approximately 560k hexahedral cells which is finer around the body.

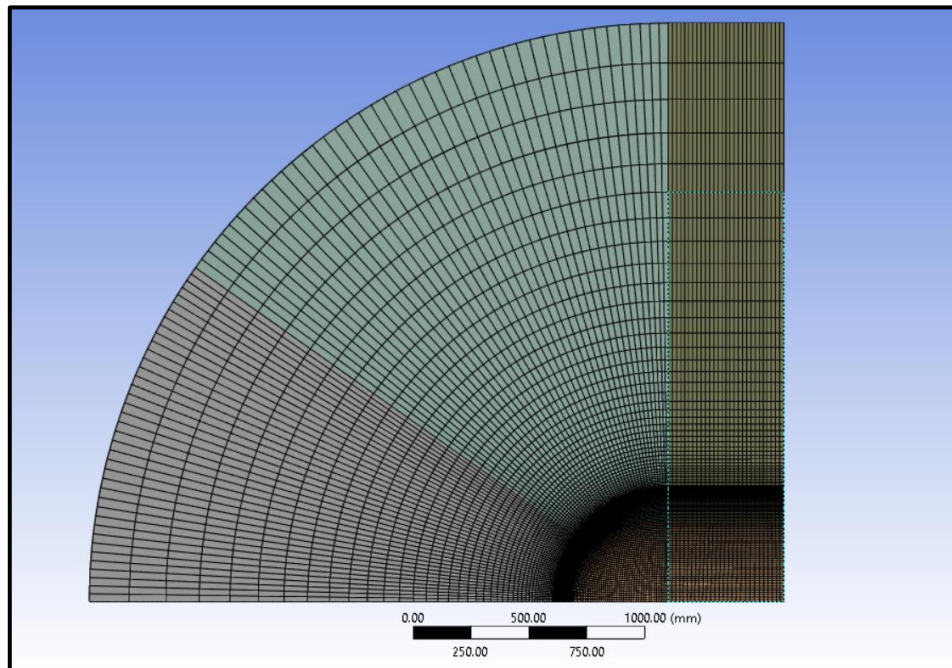


Figure 3.6 Mesh for Blunt Body

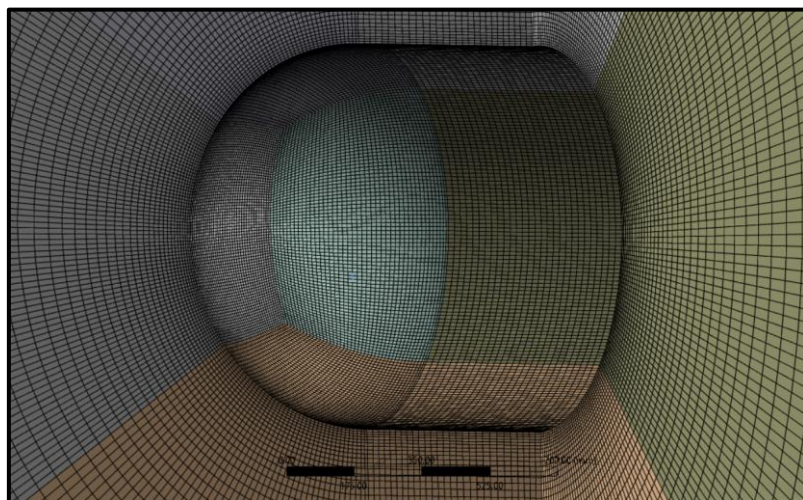


Figure 3.7 Close-up view for Blunt Body with different coloured blocking



### 3.6.2 Blunt Body with Aerospike

The following mesh for blunt body with spike consists of majority of hexahedral cells as well some prism cells totalling approximately for 790k cells.

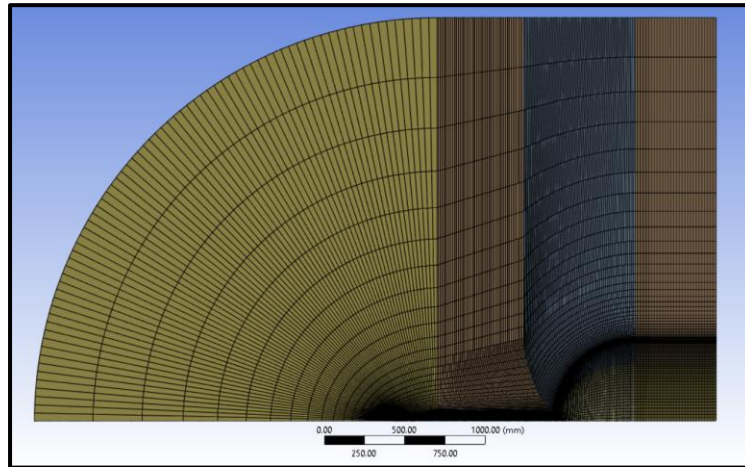


Figure 3.8 Mesh for Blunt Body with Aerospike

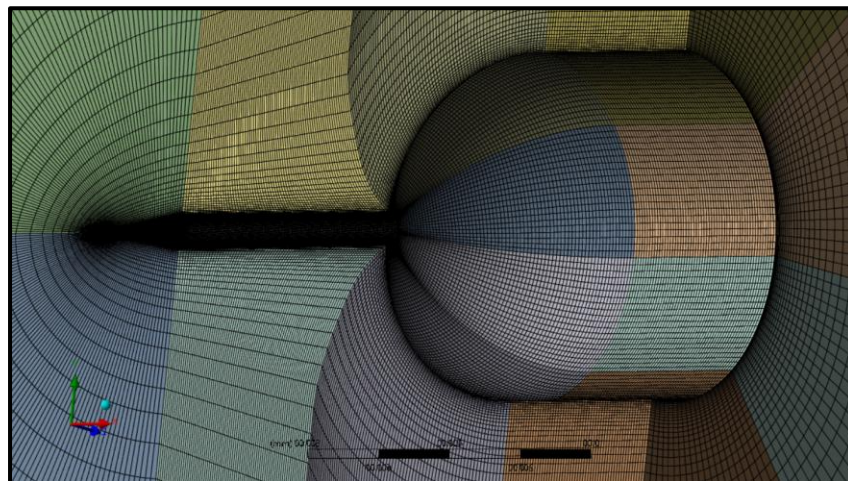


Figure 3.9 Close-up view for the Body with spike with different coloured blocking

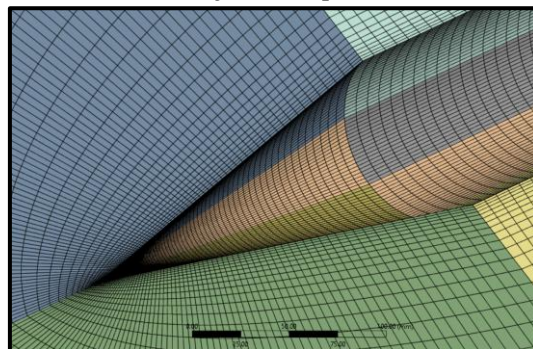


Figure 3.10 Close-up view on the pointed spike

### 3.6.3 Mesh Quality

The mesh quality report has been generated by the 'checkMesh' command in openFoam.

- Blunt Body

```
Checking geometry...
Overall domain bounding box (2.20841 -2.5 -1.08313e-16) (5.20833 2.5 2.49987)
Mesh has 3 geometric (non-empty/wedge) directions (1 1 1)
Mesh has 3 solution (non-empty) directions (1 1 1)
Boundary openness (6.02176e-16 3.34982e-17 9.96107e-16) OK.
Max cell openness = 3.32681e-16 OK.
Max aspect ratio = 9.31721 OK.
Minimum face area = 3.41105e-05. Maximum face area = 0.0105073. Face area magnitudes OK.
Min volume = 2.49725e-07. Max volume = 0.000517869. Total volume = 20.9407. Cell volumes OK.
Mesh non-orthogonality Max: 66.4287 average: 6.63817
Non-orthogonality check OK.
Face pyramids OK.
Max skewness = 0.767472 OK.
Coupled point location match (average 0) OK.

Mesh OK.
```

- Blunt Body with Aerospike

```
Checking geometry...
Overall domain bounding box (-3.23051 -2.5 -3.06093e-16) (1 2.5 2.5)
Mesh has 3 geometric (non-empty/wedge) directions (1 1 1)
Mesh has 3 solution (non-empty) directions (1 1 1)
Boundary openness (6.94312e-15 -3.58405e-16 2.27695e-15) OK.
Max cell openness = 1.19196e-15 OK.
Max aspect ratio = 366.149 OK.
Minimum face area = 2.93843e-09. Maximum face area = 0.0336733. Face area magnitudes OK.
Min volume = 4.4702e-13. Max volume = 0.00167558. Total volume = 33.0109. Cell volumes OK.
Mesh non-orthogonality Max: 78.1042 average: 16.6524
*Number of severely non-orthogonal (> 70 degrees) faces: 3360.
Non-orthogonality check OK.
<<Writing 3360 non-orthogonal faces to set nonOrthoFaces
Face pyramids OK.
Max skewness = 1.98678 OK.
Coupled point location match (average 0) OK.

Mesh OK.
```

## 3.7 Grid Independence Study

A grid independence study has been carried out for the blunt body domain at Mach number. 6.82. A grid independence study is a CFD solution that doesn't rely on the type of mesh or the size of mesh that is being used; i.e., it removes the subjectivity of the solution and makes it more general. In the current study, the size biasing is varied and the minimum size at which a general solution is obtained is used as a reference or baseline upon which mesh independence can be proved.

As we progress to make new meshes, the mesh sizing is made to be finer and finer around the body to capture the full effect of the boundary layers with the increase of mesh elements. The mesh size is reduced progressively coarse size to a fine mesh size and the variation in flow parameters is checked. When the percentage difference between the two successive meshes is negligible, the coarser mesh is finalised to be used for the rest of the simulations. Mesh independence forms an important part of CFD study to ensure that least computational resources are utilized.



For this study, four meshes were used and the size is reduced by the technique used by experts i.e., by doubling the mesh element count of the preceding courser mesh. Thus, the course mesh (A) has 140k cells, the courser mesh (B) has 280k cells, the fine one (C) has 560k cells and the finer mesh (D) contains 11.2 lakh cells. The table 3. shows the variation of the drag force on the different meshes for the blunt body domain.

Mesh Size	Drag	Result Variation %
Course (A)	1.280454e+06	-
Courser (B)	1.198591e+06	6.83
Fine (C)	1.157277e+06	3.57
Finer (D)	1.147272e+06	0.872

Table 4: Drag Force Variation in Grid Independence

As the error of drag force is quite less between the fine (C) and finer (D) mesh, the medium sized mesh of 560k cells has been chosen for the further study.

(Note: The mesh for the spiked body has been generated with the same sizes and biasing used for the Fine (C) mesh of the blunt body.)

(Note: The drag force values shown here are for half of the geometry as there is a symmetryPlane.)

## Chapter 4

### Results

(Important note: All the 2D contours observed are sliced sections of 3D simulations in the XZ plane.)

#### 4.1 Residuals

The residual is one of the most fundamental measures of an iterative solution's convergence, as it directly quantifies the error in the solution of the system of equations. In a CFD analysis, the residual measures the local imbalance of a conserved variable in each control volume. Therefore, every cell in the model will have its own residual value for each of the equations being solved. The stability and comparison of different density based solver have been explained about its accuracy in Bondarev A.E. [3] and Sean Bone's [7] researches. Figure 4.1 shows the residuals for blunt body simulation at Mach 6.82 representing that the simulation is stable and has reached a steady state.

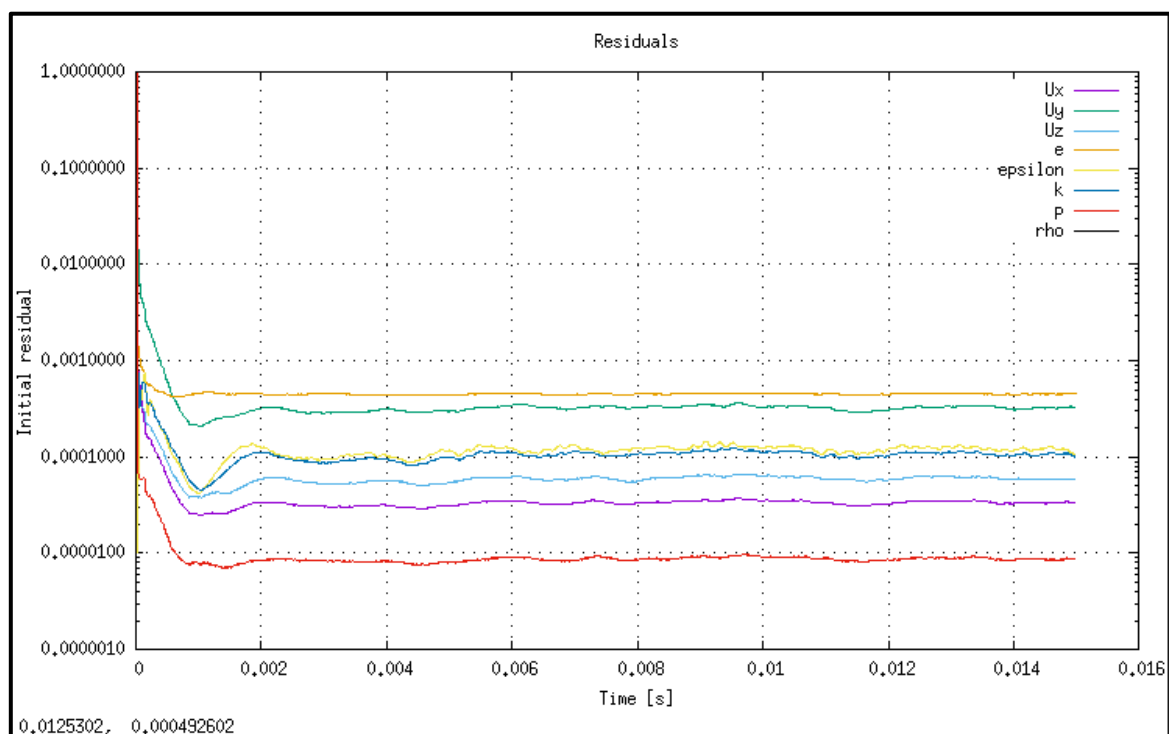


Figure 4.1 : sonicFoam's Residual Plots

## 4.2 Validation and Verification

The results for the blunt body have been validated by comparing Crawford's drag and visual shock results with that of sonicFoam's. From the analysis, the Drag Coefficients are found to out to be same with some error tolerances. Comparisons drag results are presented in Table 5, illustrating the drag results for the same Reynold's number. The agreement between the two datasets is striking, with some error observed.

sonicFoam Results	David Crawford's Results [1]
0.9156	0.85

Table 5: Comparison in Drag Coefficient Results

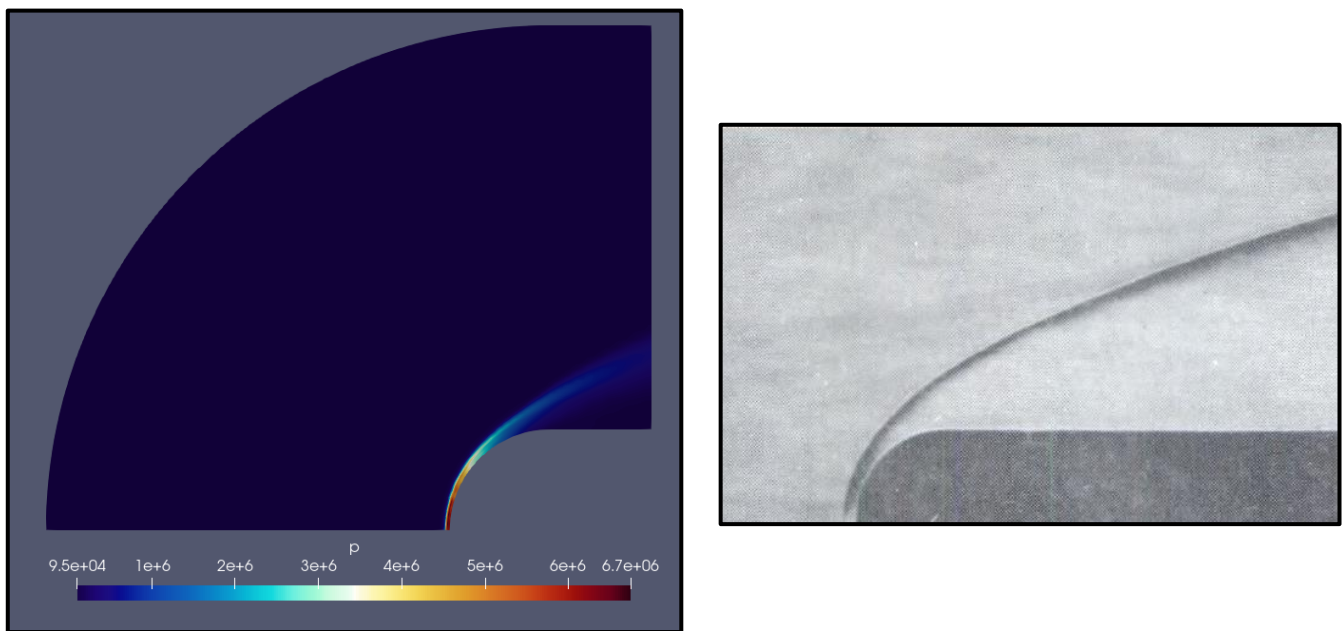


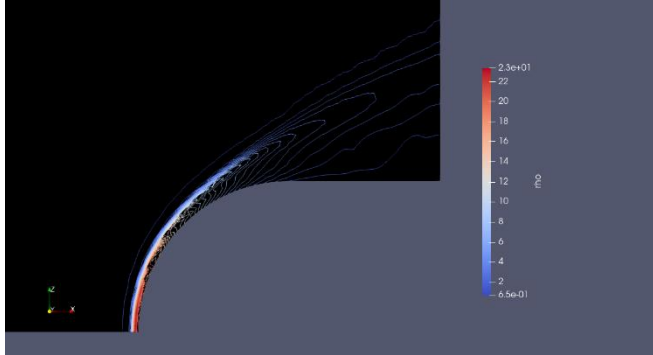
Fig 4.2: Side by side comparison of shock waves for Crawford's experiment and sonicFoam

Therefore, this validation process confirms the accuracy and reliability of our experimental findings and enhances our confidence in the applicability of the numerical model to real-world scenarios.

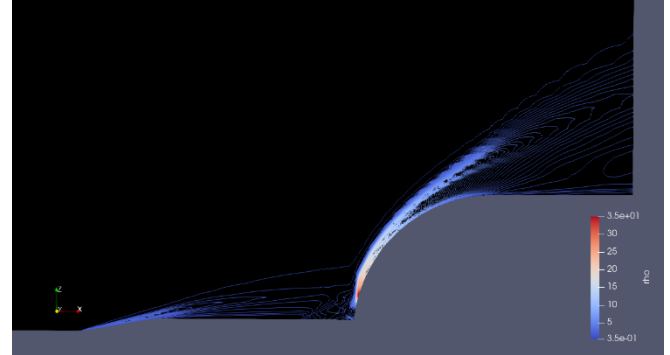
## 4.3 Shock / Density Contours

In compressible flows, the density varies and tends to be high around the boundary layers. But in supersonic free-stream conditions, shocks are formed which are abrupt and intense disturbances that travel through a medium, causing a rapid and significant change in pressure, temperature, and density. These waves create a compression front that propagates outward thus, the density of the medium increases sharply within the shock front, resulting in a higher concentration of particles in a smaller volume. This sudden increase in density is a fundamental characteristic of shock waves.

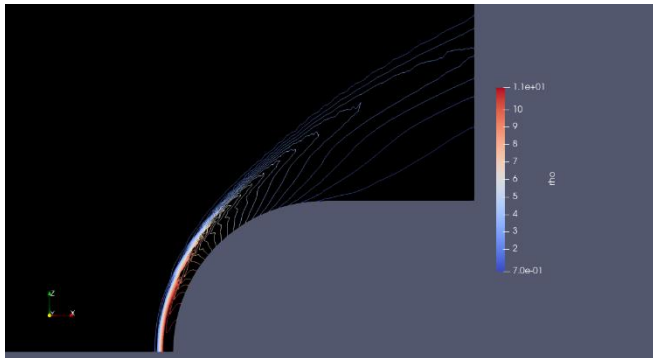
To visualize the shocks, we create density line contours by which we can understand the different shocks in better way. In the following images, we can observe the change of shock waves because of the introduced aerospike. One can also observe the variation for different Mach numbers.



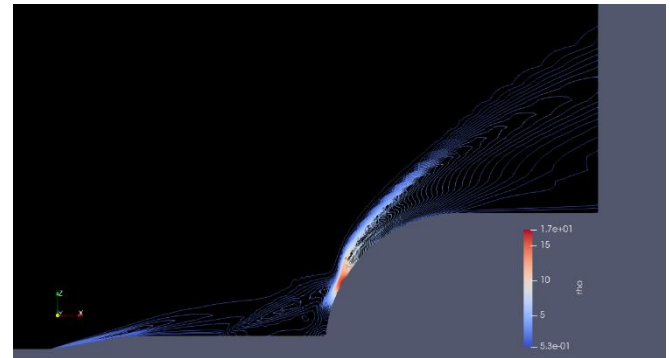
(a) Blunt Body at Mach 6.82



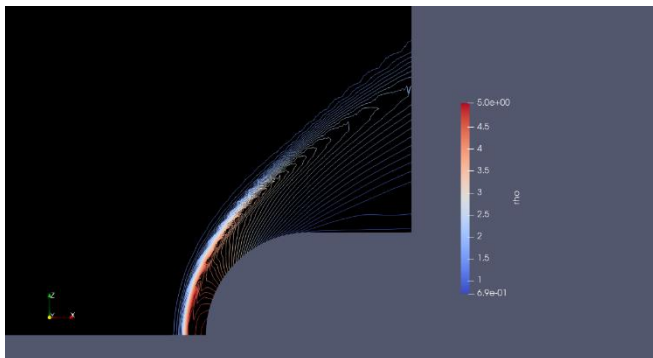
(b) Spiked Blunt Body at Mach 6.82



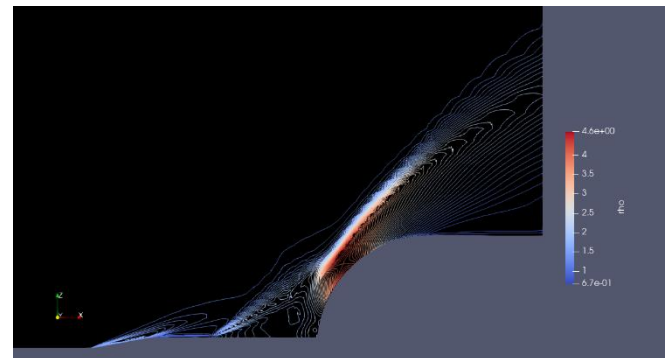
(a) Blunt Body at Mach 5



(b) Spiked Blunt Body at Mach 5



(a) Blunt Body at Mach 3



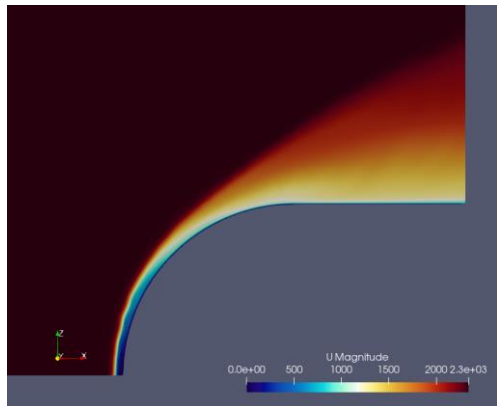
(b) Spiked Blunt Body at Mach 3

Figure 4.3: Density Contours for Blunt and Spiked Blunt Bodies at different Mach numbers.

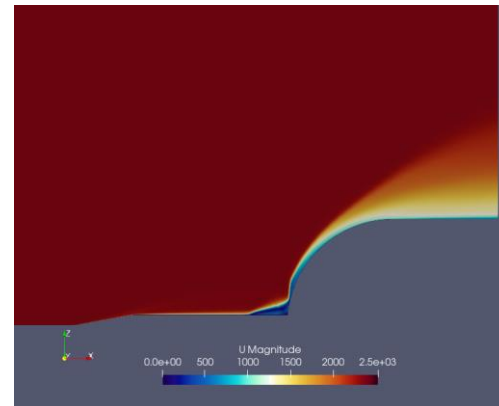
From Figure 4.3 We can observe the different shock wave formations; namely the bow shocks on the blunt bodies, the conical oblique shocks by the nose of the spike, the reattachment and the shear separations and circulations observed between the spike and the body regions.

## 4.4 Velocity over the body

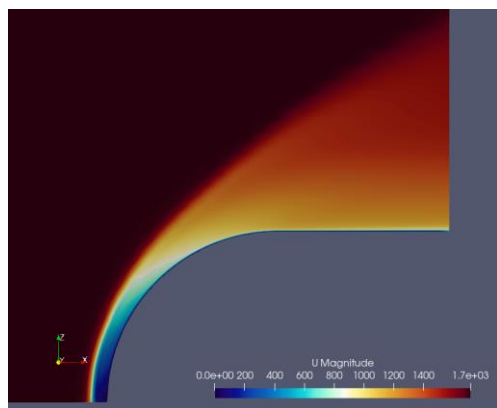
The velocity of an object over its surface plays a critical role in determining the characteristics of these shock waves. As the body's velocity increases, the intensity and strength of the shock waves generally increase as well. We can also observe that the increase in velocity also brings the shock closer to the body. Across the shocks, the velocity decreases behind the shock wave. We can also observe, that the region between the spike and body, the velocity significantly decreases as there is circulation zone formed due to turbulences.



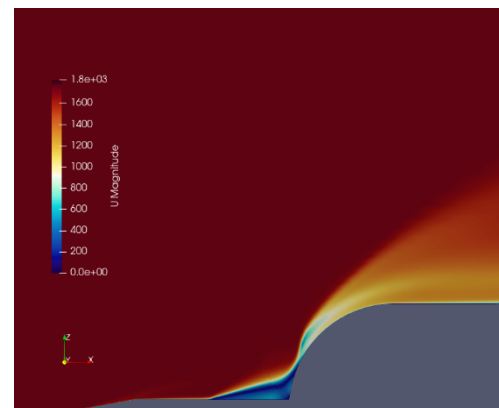
(a) Blunt Body at Mach 6.82



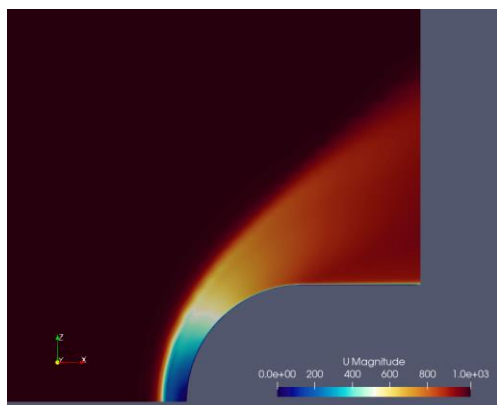
(b) Spiked Blunt Body at Mach 6.82



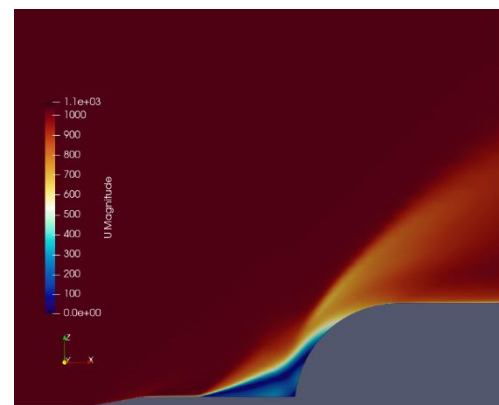
(a) Blunt Body at Mach 5



(b) Spiked Blunt Body at Mach 5



(a) Blunt Body at Mach 3

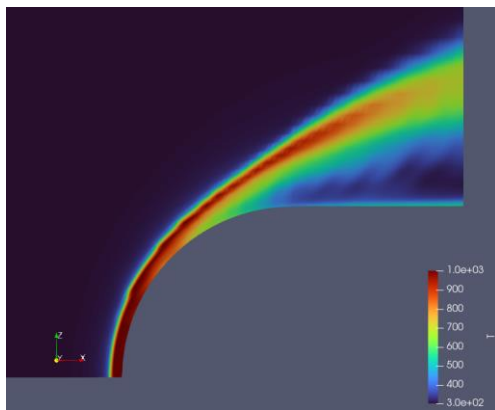


(b) Spiked Blunt Body at Mach 3

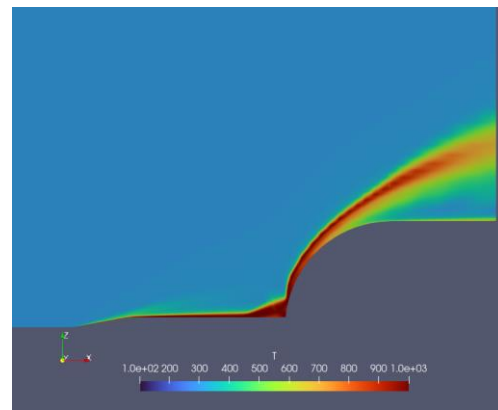
Figure 4.4: Velocity Contours for Blunt and Spiked Blunt Bodies at different Mach numbers.

## 4.5 Temperature

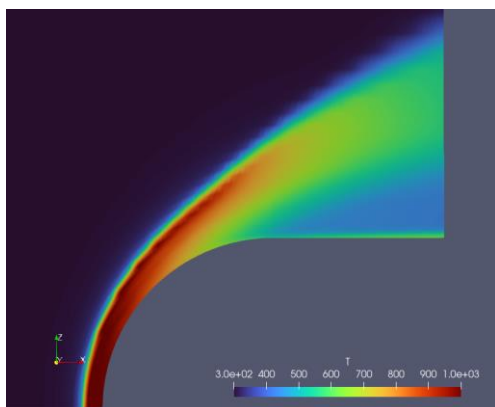
Temperature plays a very important role in the designing the nose or other structures that employ the supersonic/hypersonic body. The materials that are used in manufacturing largely depend on the surface temperatures. As such, due to the presence of shocks, the temperature is not constant throughout. Post shocks, there is a visible increase in temperature. A sharp-nosed body often heats up quickly when going supersonic. To prevent the heat reaching to the core, the body is made blunt because it can dissipate majority heat off. This technique is used for re-entry vehicles as the blunt body has higher drag and heat is dissipated off. High heating is also observed with the spike.



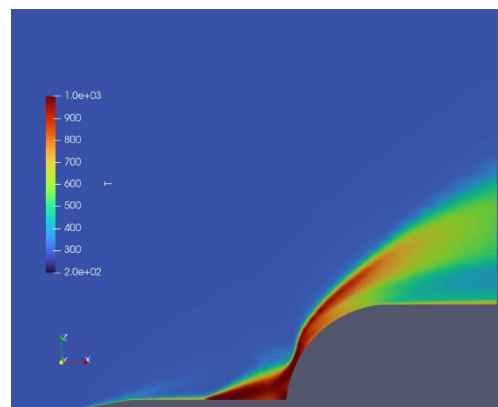
(a) Blunt Body at Mach 6.82



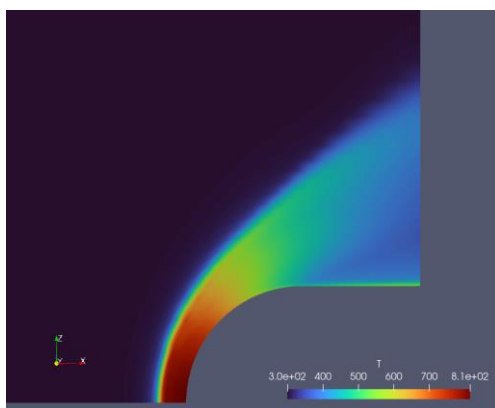
(b) Spiked Blunt Body at Mach 6.82



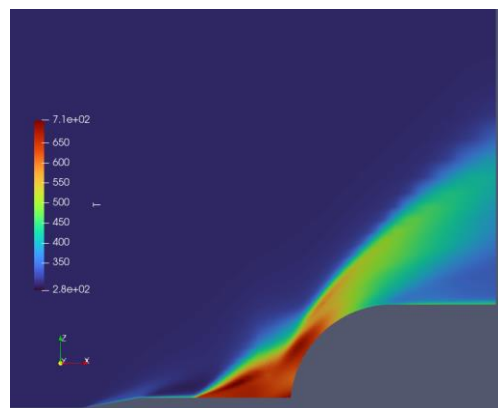
(a) Blunt Body at Mach 5



(b) Spiked Blunt Body at Mach 5



(a) Blunt Body at Mach 3

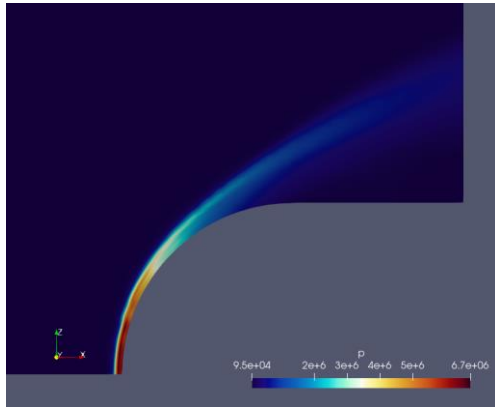


(b) Spiked Blunt Body at Mach 3

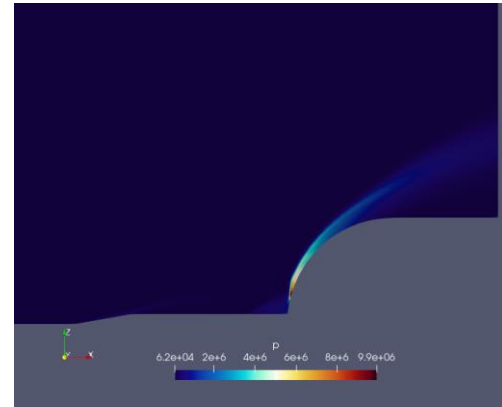
Figure 4.5: Temperature Contours for Blunt and Spiked Blunt Bodies at different Mach numbers.

## 4.6 Pressure Distribution

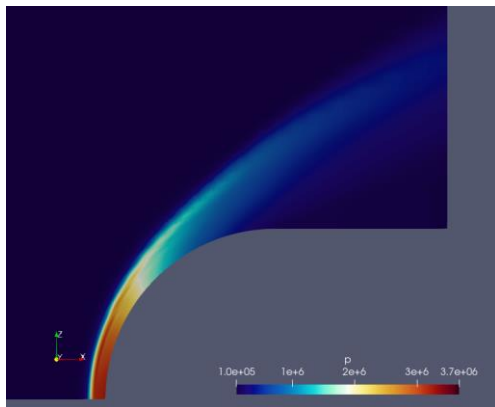
Across a shock, an increase in pressure is observed. We can observe that when the spike is introduced, the pressure drop is noticeable due to the conical detached shocks.



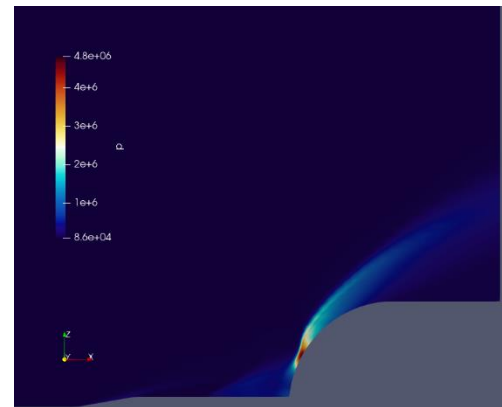
(a) Blunt Body at Mach 6.82



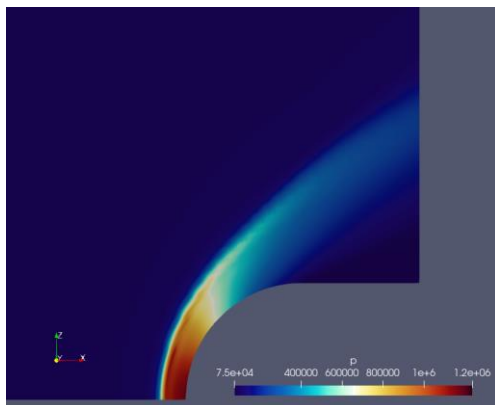
(b) Spiked Blunt Body at Mach 6.82



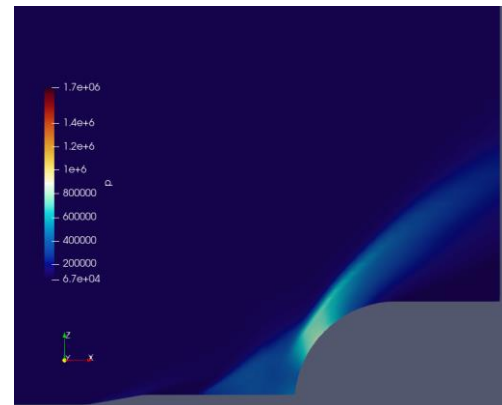
(a) Blunt Body at Mach 5



(b) Spiked Blunt Body at Mach 5



(a) Blunt Body at Mach 3



(b) Spiked Blunt Body at Mach 3

Figure 4.6: Pressure Contours for Blunt and Spiked Blunt Bodies at different Mach numbers.

The Figure 4.7 is a cumulative Pressure over the body, in which  $P/P_\infty$  is nothing but the pressure coefficient where  $P$  is the local pressure (Pa) and  $P_\infty$  is the free-stream/reference pressure which is 1 atm. On the X – axis, the co-ordinates -1 to 0 is the



spike in the front and 0 to 1 is the blunt body. For the blunt bodies, we can see the variation in stagnation pressure over different velocities. For the spiked bodies, we can observe a significant rise in pressure due to the conical shock hitting the body i.e. the reattachment zone, and then the pressure starts to drop same as the blunt bodies. One can also observe a rise in pressure in between the spike and the blunt body.

The recirculation is a critical aerodynamic feature characterized by a flow pattern where the fluid momentarily reverses its direction. In this region, the high-speed flow over the pointed spike encounters the blunt body, causing it to slow down and separate from the surface. This separation creates a zone where the airflow moves backward, forming a vortex or recirculation bubble. Understanding this recirculation region because it significantly impacts the aerodynamic forces and heat transfer on the blunt body. We analyse this flow phenomenon to optimize heat shielding, reduce drag, and enhance the overall performance of vehicles entering the Earth's atmosphere or operating in high-speed environments, such as hypersonic aircraft or re-entry vehicles.

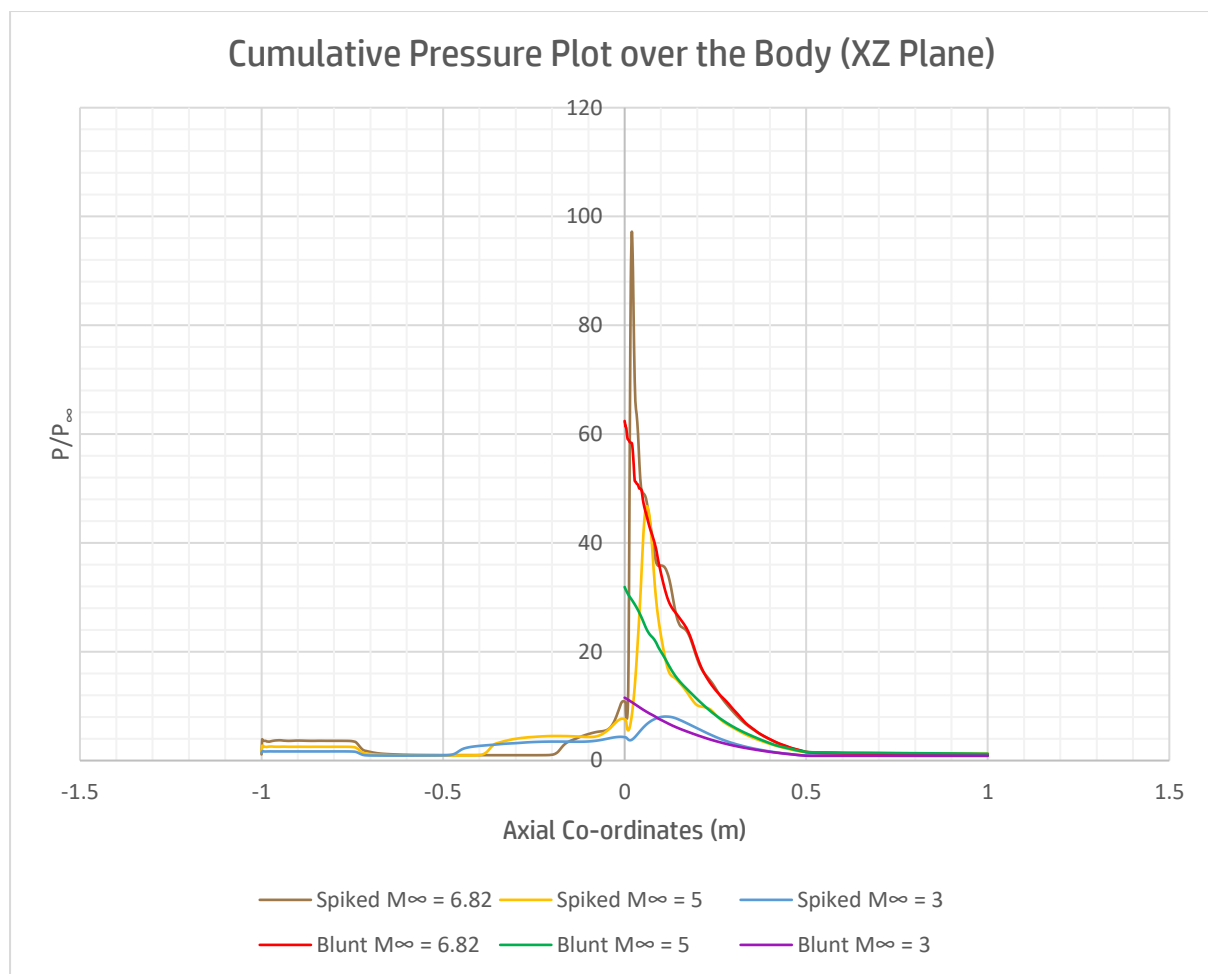


Figure 4.7:  $P/P_{\infty}$  vs X co-ordinates Plot for different velocities.



## 4.7 Drag Forces

For supersonic flight, we always need to modify our design to always has the least drag. Here, the addition of an aerospike in the front of the body detaches the bow shock, reducing the drag by creating a conical shock which the reduces drag by altering the flow dynamics and reducing the shock wave formation. As air flows over the aerospike, it accelerates and follows the shape, creating a smoother and more gradual transition from supersonic to subsonic speeds. This design minimizes the formation of strong shock waves, which are a significant source of drag on blunt bodies. By reducing shock wave drag, the aerospike configuration lowers the overall aerodynamic drag, resulting in improved vehicle efficiency and performance.

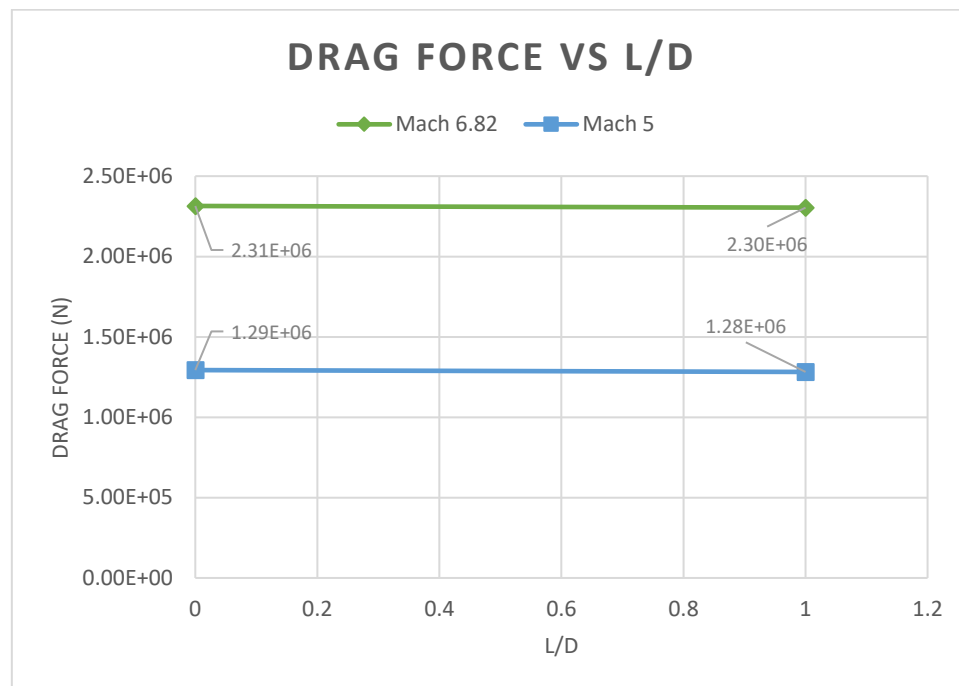


Figure 4.9 Drag Force vs L/D Plot

From Figure 4.9, we can diagnose that the error for drag is coming from the forces itself. This proves the limitation of compressible solver (sonicFoam) as per also mentioned by T. Yu [19], Bondarev [3], Sean bone's thesis [7], Luis F. Gutiérrez Marcantoni [5].

# Chapter 5

## Conclusion

### 5.1 Conclusion

A numerical study was conducted to investigate supersonic flow over a blunt body and blunt body with an aerospike. The effect of various Mach numbers which affects the Pressure distribution, Velocity profiles and Temperature was investigated. In addition, a plots of  $C_D$  vs  $L/D$ , Drag force vs  $L/D$  and Pressure Coefficient vs  $X$  coordinates was plotted. A mesh independence study was also conducted and the least computationally expensive yet accurate mesh size was determined. We conclude this paper showing the validation of Crawford's blunt body results using openFoam and further studying the blunt body with and without the aerospike in for lower Mach numbers.

### 5.2 A note on OpenFoam's Compressible solvers

The sonicFoam solver is designed for transient supersonic turbulent flow, but according to this case study results, there seem to be some limitations of the solver even while capturing drag force on spiked-blunt geometries based on the results presented. Valiyollah Ghazanfari's [8] study is also on improving the sonicFoam solver by modifying it to add more mechanical source term energy equations. Bondarev's [3] analysis on accuracy on supersonic solvers also shows rhoCentralFoam is more accurate than sonicFoam. Sean bone's thesis [7] , Luis F. Gutiérrez Marcantoni [5] etc. all these authors show that rhoCentralFoam is most accurate solver for compressible cases. Thus, this study shall be continued in rhoCentralFoam and to compare the results with Ansys FLUENT and verify Crawford's spiked body results.

### 5.3 Future Scope

In hypersonic flows, the extreme speeds and temperatures cause the air molecules to behave in a unique way. As the air encounters a blunt body or shock wave, it undergoes rapid compression and heating. At these conditions, the high kinetic energy of the molecules can temporarily dissociate them into atoms, breaking molecular bonds. However, what's remarkable is that at the micro-scale, these dissociated atoms quickly recombine into molecules due to the high collision rates and energy transfer among them. This near-instantaneous recombination process is driven by the strong thermodynamic equilibrium tendencies of the molecules. As a result, despite the initial dissociation, the air retains its molecular composition in the overall flow.

Understanding this phenomenon is crucial in hypersonic aerodynamics and propulsion, as it affects the chemistry and thermodynamics of the flow. This phenomenon greatly affects the pressure distribution around the body and contribute to heat transfers. This study can further be extended in this direction which involves thermochemistry and higher thermodynamics.

As the compressible solvers are still being constantly worked on to be precise, a comparative study on these solvers can also be conducted via this case.

## References

1. David H. Crawford<sup>1</sup>. "Investigation of the flow over a spiked-nose hemisphere-cylinder at a Mach 6.8". Langley Research Center, Langley Field, Va. National Aeronautics and Space Administration, Washington.
2. T. Chourushi<sup>1</sup>, A. Rahimi<sup>1</sup>, S. Singh<sup>2</sup> and R. S. Myong<sup>1\*</sup>. "Computational simulations of near continuum gas flow using Navier-Stokes-Fourier equations with slip and jump conditions based on the modal discontinuous Galerkin method." In: *Advances in Aerodynamics*, 2020.
3. Bondarev A.E<sup>1</sup>, Kuvshinnikov A.E.<sup>2</sup>. "Analysis of the accuracy of OpenFOAM solvers for the problem of supersonic flow around a cone" Keldysh Institute of Applied Mathematics Moscow.
4. John D Anderson Jr<sup>1</sup>. "Hypersonic and high-temperature gas dynamics." American Institute of Aeronautics and Astronautics, 2006.
5. Luis F. Gutiérrez Marcantoni<sup>a,b,c</sup>, José P. Tamagno<sup>a,d</sup> and Sergio A. Elaskar<sup>a,b,e</sup>. "High speed flow simulation using OpenFOAM." In: *Asociación Argentina de Mecánica Computacional*, 2012.
6. Muhammad Hamza<sup>1</sup>, Saima Bukhat Khan<sup>2</sup>, Saima Bukhat Khan<sup>1\*</sup>. "Geometric Optimization of Blunt Bodies with Aerodisk and Opposing Jet for Wave Drag and Heat Reduction." In: *MDPI Aerospace*, 2022.
7. Sean Bone<sup>1</sup>. "Comparative study of density-based versus pressure-based solvers for supersonic flow." Eidgenössische Technische Hochschule Zürich Swiss Federal Institute of Technology Zurich, 2020.
8. Valiyollah Ghazanfari<sup>1</sup>, Ali Akbar Salehi<sup>2</sup>, Alireza Keshtkar<sup>1\*</sup>, Mohammad Mahdi Shadman<sup>3</sup> and Mohammad Hossein Askari<sup>3</sup>. "Numerical Simulation Using a Modified Solver within OpenFOAM for Compressible Viscous Flows." Materials and Nuclear Fuel Research School, Nuclear Science and Technology Research Institute, AEOL, Tehran, Iran, 2020.
9. Senthilkumar S\*, Aarohi Anmol Mudholkar<sup>2</sup> and Sanjay K J<sup>3</sup>. "A Comparative Study on Aerodynamic Drag Reduction of a Blunt Nose Body using Aerospike and Aerodisk – Numerical Approach." In: *IOP Conf. Series: Materials Science and Engineering, ICARSES2020*, 2020.
10. Arun Kumar Chinnappan<sup>1</sup>, Malaikannan G.<sup>1</sup>, RakeshKumar<sup>\*,2</sup>. "Insights into flow and heat transfer aspects of hypersonic rarefied flow over a blunt body with aerospike using direct simulation Monte-Carlo approach." In: *Aerospace Science and Technology*, 2017.
11. Wan T\*, Liu CM. "Drag Reduction Optimization for Hypersonic Blunt Body with Aerospikes." In: *Journal of Aeronautics & Aerospace Engineering*, 2017.
12. Jiss J Sebastian<sup>a</sup>, Sandeep Eldho James<sup>a</sup>, Abhilash Suryan<sup>a\*</sup>. "Computational study of hypersonic flow past spiked blunt body using RANS and DSMC method." In: *Global Colloquium in Recent Advancement and Effectual Researches in Engineering, Science and Technology (RAEREST 2016)*, 2016.

13. Saad Ahmed, Mohammed.Samiuddin Khan, Khaja Hamiuddin Mujahid Mohd Ayazuddin, Mr. Sunil Manchala. "Report on CFD Analysis of a Spiked Blunt Body." In: *International Journal of Research*, 2018.
14. Rakhab Chandra Mehta<sup>1</sup>. "Heat Transfer Analysis without and with Forward Facing Spike Attached to a Blunt Body at High Speed Flow." In: *IntechOpen*, 2017. URL: <https://www.intechopen.com/chapters/60181>
15. Album, H. H<sup>1</sup>. "Regarding the utility of spiked blunt bodies." In: *Journal of the Aerospace Sciences*, Vol. 5, No. 1, 1968, p. 112–113.
16. R. C. Mehta<sup>1</sup>. "Unsteady Flowfield Characteristics Over Blunt Bodies at High Speed."
17. Henk Kaarle Versteeg<sup>1</sup>, Weeratunge Malalasekera<sup>2</sup>. *An Introduction to Computational Fluid Dynamics: The Finite Volume Method*. Pearson Education Limited. (2007)
18. R. C. Mehta<sup>1</sup>. "Heat Transfer Analysis without and with Forward Facing Spike Attached to a Blunt Body at High-Speed Flow ". 2017
19. T. Yu<sup>1,2</sup>, Y. Yu<sup>1,2,3†</sup>, Y. P. Mao<sup>2</sup>, Y. L. Yang<sup>1,2</sup> and S. L. Xu <sup>2</sup>. "Comparative Study of OpenFOAM Solvers on Separation Pattern and Separation Pattern Transition in Overexpanded Single Expansion Ramp Nozzle". In: *Journal of Applied Fluid Mechanics*, Vol. 16, No. 11, pp. 2249-2262, (2023).